JOURNAL OF PROPULSION AND POWER
Vol. 25, No. 1, January–February 2009

Fracture Mechanics of Composite Solid Rocket Propellant Grains: Material Testing

Giuseppe Sandri Tussiwand*
MBDA Bayern-Chemie, GmbH, 84544 Aschau am Inn, Germany
Victor E. Saouma†
University of Colorado at Boulder, Boulder, Colorado 80301-0428
Robert Terzenbach‡
MBDA Bayern-Chemie, GmbH, 84544 Aschau am Inn, Germany
and
Luigi T. De Luca§
Politecnico di Milano, 20153 Milano, Italy

DOI: 10.2514/1.34227

Following a detailed literature survey on the fracture-mechanics properties of solid rocket propellants, this paper reports on an innovative set of fracture tests performed on a composite solid propellant based on ammonium perchlorate hydroxyl-terminated polybutadiene. After a short summary on standard linear–viscoelastic mechanical characterization, results on both linear–elastic fracture-mechanics (characterized by the fracture toughness K_{IC}) and nonlinear fracture-mechanics (characterized by G_F) tests are reported. Test results for linear–elastic fracture-mechanics simulations have been obtained using middle-tension specimens. A practical methodology to separate the amount of strain energy lost through viscous processes from other sources is given and provides an effective method to apply the toughness-test validity criteria of the American Society for Testing and Materials E399 norm to propellants and other thermoviscoelastic materials. Measurements to determine the linear fracture-mechanics properties of the propellant have been carried out applying the wedge-splitting test methodology. Master curves for the toughness, the critical crack-opening displacement, and the fracture energy have been generated to correlate test data. Results are coherent with Shapery's theory of fracture for viscoelastic materials. Results can be used within finite element simulations to assess the safety and integrity of a solid-propellant rocket motor under various loads, such as thermal cycling and ignition, assuming stationary conditions.

Nomenclature

A_{lig}	=	ligament area in a wedge-splitting test specimen torn apart by the advancement of the crack
a	=	crack length
a'	=	speed of crack propagation
a_T	=	time–temperature shift factor
$D(t)$	=	creep compliance
D_0	=	glassy compliance
$E(t)$	=	stress-relaxation modulus in tension
E_R	=	reference modulus in the principle of correspondence
E_∞	=	limit stiffness for a linear–viscoelastic material (time to infinity because load application)
E'	=	equal to E in plane-stress conditions and to $E/(1-\nu^2)$ in plane-strain conditions
F_S	=	horizontal splitting force in the wedge-splitting test
f'_t	=	fictitious crack model's peak stress in the fracture process zone
G	=	energy release rate per unit crack extension
G_F	=	fracture energy in the fracture process zone
J_v	=	viscoelastic J integral
K_I	=	mode I stress intensity factor (in plane strain)
K_{Ic}	=	critical stress intensity factor in mode I
$P_{\max}$	=	maximum measured load in a test
P_Q	=	maximum load in a tensile test computed with the linear–viscoelastic material model
P'_Q	=	maximum load in a tensile test computed with the American Society for Testing and Materials E399 standard
s	=	displacement
sup	=	supremum
W_F	=	work of fracture performed by a testing machine on a wedge-splitting test specimen
δ_c	=	critical crack-opening displacement
ε	=	strain
ε'	=	strain rate
σ	=	stress
ω	=	strain energy (density)

Subscripts

corr	=	corrected (stress) assuming incompressibility
max	=	maximum

Received 23 August 2007; revision received 27 June 2008; accepted for publication 5 September 2008. Copyright © 2008 by the American Institute of Aeronautics and Astronautics, Inc. All rights reserved. Copies of this paper may be made for personal or internal use, on condition that the copier pay the $10.00 per-copy fee to the Copyright Clearance Center, Inc., 222 Rosewood Drive, Danvers, MA 01923; include the code 0748-4658/09 $10.00 in correspondence with the CCC.

*Throtteable Ducted Rocket Development, Liebigstrasse 15-17. Member AIAA.
†Professor.
‡Senior Laboratory Technician, Physical Test Laboratory, Liebigstrae 15-17.
§Professor, Laboratorio di Propulsione Aerospaziale, via La Masa 34.

Introduction

STATE-OF-THE-ART solid rocket motors for tactical and space applications use a grain made of composite propellant, a solid energetic material containing oxidizing and fuel chemicals that react at explosive rates, releasing thermal energy and sustaining stable deflagration until the material is decomposed.

The rocket motor achieves its mission only if the combustion and regression of the grain proceeds as expected, following a regular surface evolution in time, as predicted by a simulation of internal

ballistics during the design phase. If this is not the case, the consequences range from an unexpected case pressure and thrust evolution to a catastrophic failure of the motor through a burst or burn-through of the case, involving loss of mission, equipment, and possibly human lives. The evaluation of structural integrity of the grain at ignition, where it is subjected to critical loads, is therefore one of the critical activities to be performed to satisfy requirements of safety and reliability of operation set by the end user.

Much effort is therefore put in the prediction of the stresses, strains, and displacements induced by the various loads acting on the grain during its service life. This is typically achieved through a finite element analysis, implementing a constitutive law sufficiently accurate to account for the complex linear–viscoelastic behavior of the propellant [1–3]. Significant mechanical testing efforts are generally needed to calibrate the material model, and the problem is further complicated by the fact that chemical and mechanical aging change the constitutive properties of the propellant [2–5] after manufacturing and they do so differently for each individual motor.

Once the induced stresses and strains are predicted, it is necessary to decide whether they exceed the mechanical capability of the propellant and to formulate a measure of the grain's structural reliability in terms of a safety factor or a probability of failure at ignition [2,6]. A common approach is to assume that the grain is unflawed, characterize the unaged material, and apply a strength-based approach to compute the reliability; that is, compare a scalar function of the induced stress/strain tensors in the grain in which the loads are the highest with a limit value of the same scalar determined through conventional failure tests on material specimens. Typical failure criteria used in common practice are, for instance, the maximum principal strain criterion, the Stassi–Mises criterion, or the von Mises criterion [2].

The strength-based approach alone is, however, insufficient in the following cases:

1) Conventional finite element analysis (FEA) predicts an insufficient margin of safety in a very limited region of the grain. The probability of a local crack forming at this spot is beyond the maximum values specified for the motor. However, even if it occurred, such a local collapse does not necessarily imply a failure of the motor.

2) The grain exhibits flaws after manufacturing. Flaws can be voids or cracks embedded in the propellant or cracks at the free surface of the grain. The motors can be either regrained or fired, and results are used to generate a catalogue of tolerable flaws for motor acceptance after manufacturing. There are several problems posed by this approach, among which are the following: there is no guarantee that the flaws will not propagate during service life, and flaws might be present but not detected if they are smaller than the resolution of the available diagnostic system.

3) Mechanical aging, possibly enhanced by chemical aging, reduces the capability of the propellant, finally generating a crack in the grain. Thermal cycling (occurring during day–night and seasonal temperature variations or captive carriage) can propagate small cracks until a critical size is reached for the motor [7–9] if the propellant is brittle or made brittle by chemical aging. Typically, the motor is decommissioned and a safety evaluation which can include firings needs to be performed. Results are used empirically within surveillance programs, but cracks are rarely identical and motors are rarely exposed to exactly the same environment; for the same reasons listed previously, there is no guarantee that motors with similar flaws will have the same safety of use.

The procedure of assessing safety and reliability of motors exhibiting flaws after manufacturing or some deployment time by a small number of static firings or other full-scale tests [10] to build up a flaw catalogue is clearly unsatisfactory in terms of safety and costs. First, the success or failure of the firing of a motor with a grain with a specific flaw is actually a matter of probability. There is no guarantee that another firing would succeed, and the only way to find out would be to fire many motors with exactly the same flaw: an impossible and impractical task. Second, the propellant of each grain actually has individual mechanical properties because of batch-to-batch variations and different aging conditions, which changes both the constitutive and the failure properties of the propellant. Therefore, a motor with a specific crack might perform well, and the next one might fail if it has been exposed to a different, more benign, environment and its mechanical properties are randomly better due to batch-to-batch variations in mechanical properties.

Results obtained for a small number of motors within surveillance or after manufacturing will not be representative for the entire stock [11]. Furthermore, test conditions for static firings might not be representative of the conditions encountered during use. Finally, even if many flawed motors had been fired during development or in the production/deployment phase, success is neither necessary nor sufficient to determine the safety and reliability of use for the rest of the stock. A more efficient and safe approach requires a rational combination of simulation and testing, as it is normally done with unflawed motors; simulation activities need to be supported by appropriate material testing procedures and to be validated adequately, after which they can be used predictively [12].

The application of fracture mechanics should be mandatory in the cases listed previously, because any strength-based failure criterion becomes potentially conservative if the crack size is large enough [2,13], its position and orientation are dangerous, and/or the propellant is brittle. Moreover, conventional FEA produces inconsistent results near the tip of a crack [13]: any conventional failure criterion is locally violated and informative, and standard meshing gives inconsistent results even if the element size is very fine. In the presence of a crack or flaw, one needs to assess whether the crack size is critical at ignition and would produce failure of the solid rocket motor (SRM) [2,12] by excessive propagation, and, if not, whether the crack size, possibly propagated to some extent by the ignition load, will change the internal ballistics of the motor in an unacceptable way [14–17]. In any case, one needs to assess whether or not the structural reliability of the grain is determined by the crack size or by a classic strength-based approach; this can be accomplished only by completing conventional FEA with a fracture-mechanics-based analysis.

Another point is now mentioned: although in the presence of a crack in a heterogeneous material, conventional failure criteria are either inapplicable or not conservative, the opposite is also true (cf. the motor firings reports in [2]) if the propellant has good fracture resistance and a low ballistic exponent. In this case, when local failure evolves in the generation of a crack or one is present before ignition, limited propagation can occur, in agreement with conventional failure criteria and classic fracture mechanics (K_I vs K_{IC}), but the crack will not propagate enough to appreciably alter the internal ballistics of the motor. Application of such failure criteria to flawed-motor acceptance or in the SRM design phase is therefore overly conservative. Reducing the web fraction of the SRM following such a prediction is detrimental to performance. Therefore, there is a margin for performance and safety improvement if better failure prediction criteria are applied and classic criteria are integrated with fracture mechanics.

This work aims at determining the critical crack size for a centrally perforated grain (such as the segment of a space launcher booster or a nozzleless motor for tactical applications) applying finite element analysis and using a linear and a linear fracture-mechanical model for the material; it focuses on the fracture mechanics of a grain, and pressure is assumed to be stationary. Input data for the analysis was generated using an extensive test campaign described in this paper.

Literature Survey

Considering the topic of fracture mechanics of elastomers and propellants, theoretical approaches were published by Knauss [18] and have been completed in a general theory by Shapery [19–21]. Shapery extended the J-integral theory of Rice and Brobery, as summarized by Anderson [13], to time-dependent materials through the principle of correspondence, by associating a pseudosolution following the equations of linear–elastostatics to the original viscoelastic problem using Laplace transforms or, to simplify, an equivalent elastic stiffness that depends on load and temperature

history [19]. Previous approaches developed for time-dependent materials such as metals subjected to creep turn out to be a special case of Shapery's J_v integral theory. The theory is based on Dugdale's [22] and Barenblatt's [23] approaches of a process zone ahead of the true crack characterized by cohesive stresses and gives general equations for the size of the damage zone and the relationship between damage-zone loads and the speed of crack propagation. To the authors' knowledge, the earliest experimental verification using composite solid propellants occurred almost at the same time and is due to the work of Buswell [24], followed by a complete critical examination carried out by Swanson [25]. After these remarkable developments, the theory was expanded to the general case of viscoelastic materials with temperature-dependent properties and strain-dependent linearities [26].

Fracture-mechanical properties of a polybutadiene-acrylonitrile (PBAN) binder system and composite-modified double-base propellants were measured by Beckwith and Wang [27] in the second half of the 70s. Bencher et al. [28] characterized an inert formulation based on a hydroxyl-terminated polybutadiene (HTPB) binder system at 3 different temperatures and slow strain rates. In addition to J_v–a resistance curves, their paper describes the morphology of a failure process zone in a solid rocket propellant: in particular, its formation and evolution until collapse. Langlois and Gonard [29] published results obtained using polyurethane and carboxyl-terminated polybutadiene propellants. Most experimental work on the fracture mechanics of ammonium perchlorate (AP)-HTPB-based solid propellants has been performed by Liu [7,8,30]. He published results on experimental crack-resistance curves following a linear–elastic fracture-mechanics (LEFM) approach, pointed out the dependence of these curves on temperature and strain rate at typical application temperatures and slow-to-moderate strain rates, and performed crack-velocity-vs-load experiments (K_I vs a') as well as subcritical crack-propagation experiments. The application of fracture mechanics to predict the service life of a motor and the determination of the critical crack size as an acceptance criterion for high-cost SRMs has been partially published in [12].

Direct simulation on a system level (i.e., coupling the fracture-propagation problem with the internal fluid dynamics of a motor during combustion) has been tackled by Smirnov and Dimitrienko [31], Kumar and Kuo [15], Lu and Kuo [16], and Lu et al. [17] using data on a AP-PBAN-Al propellant within research activities carried out for a structural-ballistic risk-assessment methodology program. More recently, coupled simulation results were published by one of the working groups of the centers for the simulation of advanced rockets [14].

The methodology adopted for the linear material characterization used in this study borrows heavily from previous work of the second author [32,33]. As a matter of fact, the problem being considered bears great similarities with the behavior of concrete dams. Slowik et al. [34] investigated the fatigue crack growth in cementitious materials (equally characterized by the presence of cohesive stresses along the fracture process zone). It was determined that constant-amplitude fatigue loading resulted in an erosion of the fracture process zone, whereas the crack tip does not advance. Eventually, if there is no increase in the load magnitude, there is no more crack propagation. For this to occur there has to be an increase in the load (thus variable-amplitude loading), which will in turn create a new virgin fracture process zone (FPZ). Composite solid propellants exhibit the same behavior as reported by Liu [8,30] and found in this work. It seems that a common characteristic of heterogeneous materials with a softer matrix is the formation of a FPZ characterized by cohesive stresses at the tip of any crack. Wedge-splitting test (WST) testing, a characterization methodology developed for concrete, was applied to a composite propellant within this study and it was noticed that, as with concrete, the driving force during the test peaks as a process zone at the tip of the crack is fully formed and then drops when the crack starts to propagate in the propellant specimen.

Along with all this background information, the experience accumulated with different propellant formulations during several years at the propulsion laboratory in Milan and a chemical background on the compounding of an AP propellant with a HTPB-isocyanate binder system proved to be extremely valuable to the test program and to the understanding of the observed phenomena.

Conventional Mechanical Properties

The composite propellant used in this study belongs to the most employed family used for solid rocket propulsion applications. A composite solid propellant is a heavily filled elastomer containing a distribution of rigid particles (typically AP particles as oxidizer and metal particles as fuel). They make up about 90% of the mass. The binder is usually a polyurethane elastomer using HTPB as the base polymer, networked with a polyfunctional-isocyanate. Further additives play a fundamental role in the mechanical properties: the plasticizer is an organic oil depositing itself between the binder chain segments, facilitating mutual shearing through weakening of the van der Waals bonds existing between different atoms of the chain segments, and the bonding agent is a hybrid molecule, containing functional groups that react both with the rigid inorganic AP particles and the binder, establishing strong ion bonds between the rigid inclusions and the binder itself. The specific formulation used here is a fast-burning-rate medium-elongation material based on AP, using about 10% HTPB, with a low content of aluminum, which is typical of tactical propulsion applications.

Standard Linear–Viscoelastic Characterization

The constitutive behavior of a propellant is strongly thermo-viscoelastic [1,2], and the amount of mechanical energy dissipated by rearrangements on a molecular scale depends on the strain rate and temperature of the material. This affects material failure in the process zone of a crack as well as in the bulk propellant, because the propellant fails by microcrack generation and propagation into the binder or at the binder–inclusion interface [35]. As a result, fracture-mechanical properties and conventional failure properties of the propellant depend on strain rate and temperature.

A standard linear–viscoelastic (LVE) characterization provided information on the constitutive properties for the simulation of cooling and ignition pressurization loads, as well as some hints on what to expect from fracture-mechanical testing. First, a relaxation-modulus master curve was generated using standard relaxation tests at 3% strain in tension, following the STANAG 4507 [36] norm in a temperature range between −60 and +80°C. Unlike in [28], it was found that the strain level at low strain does affect the material stiffness [2,35], probably because of Payne-effect mechanisms affecting the heavily filled elastomer [37]. Therefore, strain sweeps using a dynamic-mechanical analysis (DMA) tester were performed to make sure that a stable stiffness-strain range was reached before performing relaxation tests. The relaxation-modulus master curve was fitted with a Prony series using a linear least-squares procedure [1]. The time–temperature superposition behavior was modeled using the Williams–Landel–Ferry (WLF) equation [1,2,6,38]. The shift factors between −55 and 71°C were determined shifting both the stress-relaxation curves and the storage and loss moduli obtained from dynamic-mechanical analysis. Measurements of the glass-transition temperature range at different frequencies using DMA and differential scanning calorimetry, together with an estimate of the earlier onset of glass transition at higher frequencies using the method provided in [38], indicated that the onset of glass transition at high frequencies or high strain rates occurs as early as between −40 and −50°C. Therefore, two sets of WLF parameters were generated to fit the shift factors: one valid between −40 and 71°C and another one between −40 and −55°C, following Ferry's [38] suggestions. Correlation proved to be satisfactory, as was the matching of the shift factors obtained from stress-relaxation tests in tension and DMA.

The conventional failure properties of the propellant were measured using uniaxial "dog-bone" samples following the STANAG 4506 norm [39] in a strain-rate range between 0.01 and 2000 mm/ min. Master curves for the strain at maximum stress, the maximum stress, and the modulus at 5% strain were generated using the shift factors measured previously. The trends are typical of AP-HTPB propellants and will not be shown in detail: the strain

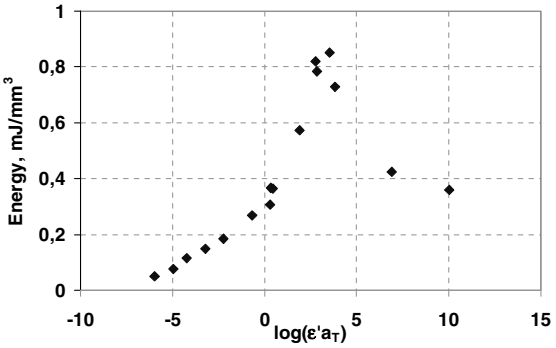

Fig. 1 Master curve for the strain energy (density) at maximum stress, calculated as $\omega = \frac{1}{2}\sigma_{\max\cdot\mathrm{corr}} \cdot \varepsilon$.

capability increases starting from the rubbery elastic region at high temperature and slow strain rate (where it amounts to about 30–40%); at higher reduced strain rates it reaches a peak and then drops relatively fast as the glass-transition range is approached and entered. On the contrary, the strength increases monotonically by about tenfold starting from values around 1 MPa at slow reduced strain rates. As a result, the specific strain energy at fracture is low at a low reduced strain rate, reaches a peak, and drops. The peak is delayed with respect to the peak in strain capability and occurs when the drop in strain capability exceeds the increase in strength (i.e., within glass transition). A graph of the specific strain energy at maximum stress summarizes the conventional failure properties of this material and is shown in Fig. 1.

Other Effects

A database of the properties discussed in the previous section must also be collected to perform a LVE analysis of the grain and is generally available and useful to fracture-mechanical testing and analysis. On top of that, constitutive and failure properties' dependence on several linear effects cannot be neglected. An important feature is their dependence on the state of stress: in particular, the amount of superposed hydrostatic pressure [1–3,6,40,41]. Failure is initiated on a microscopic scale by cavitation in the matrix near the particles [35,42] or at the matrix–filler interface; this is typical of heterogeneous materials with a finite adhesion stress between a more rigid phase, such as the oxidizer particles for a propellant and the stone filler in concrete, and a softer phase constituting the matrix. In addition to composite solid propellants, other examples are soils and cementitious materials. The presence of a state of hydrostatic pressure in the material improves the failure properties by delaying or suppressing the onset of cavitation [2,35]. Another effect influencing failure properties of elastomers is prestrain, which produces orientation of the binder molecules in the load direction, thereby changing the mechanical properties. To take both effects into account and measure the mechanical properties for the ignition load cases analyzed, additional uniaxial tensile tests using dog-bone specimens were performed under pressure and prestrain.

The data obtained under prestrain and pressure can be further used for fracture-mechanical analysis and testing. because the strength is one of the parameters characterizing the failure model of the cohesive elements employed in the crack FPZ scheme, a preliminary calibration of the nonlinear fracture-mechanics (NLFM) model chosen for the pressurization load cases required strength and modulus data obtained under realistic conditions. In particular, the cohesive elements' failure is modeled with a Mohr–Coulomb failure envelope [32], and failure properties with prestrain and pressure were used to determine the material strength for preliminary calculations on the ignition pressurization load cases.

Application of Conventional Properties to Fracture-Mechanical Analysis

With respect to a LEFM approach, it was important to decide whether the K_{IC} data obtained during testing were valid according to the American Society for Testing and Materials (ASTM) E399 standard. A suggestion by Anderson [13] was followed: the standard prescribes a maximum amount of stiffness drop caused by plasticity before crack propagation. However, because the material is viscoelastic, it was necessary to discriminate between the stiffness drop caused by viscous relaxation and the drop caused by true damage. This was done by calculating the intrinsic stiffness decay caused by relaxation through a simulation of a tensile test at the same conditions. For that, the relaxation-modulus master curve obtained within LVE characterization had to be used. This approach seems equivalent to that adopted during the J-testing performed by Bencher et al. [28], who calculated the amount of load-line displacement due to creep during the tests using Shapery's J_v methodology and the principle of correspondence [19].

LEFM Testing: K_{IC} Measurements

If the assumptions of LEFM hold, the strain energy loaded in the crack is dissipated in a small zone at the tip of the crack. The stress field at the crack can be characterized by a vector for which the components are the stress intensity factors for opening, sliding, and tearing in 3-D or just opening and sliding in 2-D. The stress intensity factor in mode I (opening), K_I, is by far the most critical with respect to propagation for an isotropic material. The critical value of K_I triggering propagation under plane-strain conditions is a material property (K_{IC}, or toughness) and can be measured using one of the standard geometries specified in the ASTM E399 test method [43]. This value is taken as a scalar capability index and compared with the value of K_I induced by the loads after a LEFM analysis of the solid-propellant grain using the finite element method.

Therefore, the first objective of the toughness measurements on the propellant was to obtain fracture-toughness data to be used as an index of material capability for the structural assessment of a cracked solid-propellant grain (LEFM approach). Second, the aim was to explore the influence of strain rate and temperature on the toughness and to verify the applicability of the master curve methodology to the correlation of experimental data on this property. Some trends could actually be expected using the information provided by [8,28–30]. In particular, because the conventional failure properties of the material depend on strain rate and temperature, the same was expected to happen with the fracture-mechanical failure properties. Several authors published evidence for this in the past [8,28,29].

Specimen Geometry

The requirements driving the specimen's geometry were the ease and accuracy of manufacturing, safety issues during testing, and achievement of plane-strain conditions. Of the five standardized geometries for metals indicated in chapter 7.1.1 of [13], only the middle-tension (MT) panel and the single-edge notched bend (SENB) specimens can be manufactured without milling the propellant, which requires a remotely controlled, explosive-safe milling machine. Alternative choices are the single- (double)-edge notched-tension specimen geometry used by Langlois and Gonard [29] or the edge-cracked panel used by Liu [8,30]. Another decisive advantage of these geometries is that the grips of the hydraulic tensile machine do not have to be fixed to the sample through some holes in the propellant. Because the material at high temperature is very soft, this would cause significant measurement errors in terms of the displacement on the material. The MT specimen was preferred to the SENB because the hydraulic machine had an elongated climate chamber for testing at cold temperatures, so that larger samples could be used if the length of the specimen was aligned with the loading direction of the machine. Another advantage is that the MT specimen could be conveniently used for subcritical crack-propagation measurements, so that it was possible to verify the validity of the LEFM approach by observing whether cyclic loaded samples used for fatigue testing failed when the crack length and the load matched the critical values measured during the K_{IC} test. Bencher et al. [28] made the same choice.

Table 1 MT specimen geometries used for testing

Sample type	Application	L, mm	$2a$, mm	$2W$, mm	B, mm
MT panel type 1	K_{IC} test	75–77	12.44	24–25	11–12.5
MT panel type 2	K_{IC} test	40–42	5.02	12–13	9
MT panel type 3	Mode I fatigue	75–77	5.02	24–25	11–12.5

Sample Preparation

The samples were die-cut out of propellant slabs to match the required geometry. The sizes used for these measurements are summarized in Table 1 (cf. Fig. 2).

Although it would have been interesting to use different specimen geometries and check if the K_{IC} values would turn out to be the same, it was decided to test the propellant using the same specimen geometry and scale it to check whether K_{IC} depends on the specimen's size. The thickness of the specimens was selected to be at least about half the width ($B \approx W$) for type 1 geometry and 70% of the total width for type 2, to determine if test results would exhibit a thickness dependence. It was not necessary to cycle the specimen to produce a sharp crack in the material; two razor-sharp blades of the required length were manufactured and used for the purpose (Fig. 3). Their thickness was 300 μm, comparable with the size of the larger oxidizer particles, so that the notch produced through the blades could be assumed to be as sharp as a crack obtained by a preliminary subcritical cycling stage. Moreover, in addition to being time-consuming, subcritical cycling would alter the stiffness of the material ahead of the crack (Mullins effect [4]) and produce orientation, thereby potentially changing the toughness ahead of the crack. To suppress displacement at the grips of the test machine, the MT specimens were tabbed through a stiff epoxy glue cast into aluminum cylinders (Fig. 4). Results proved to be quite reproducible (cf. Table 2).

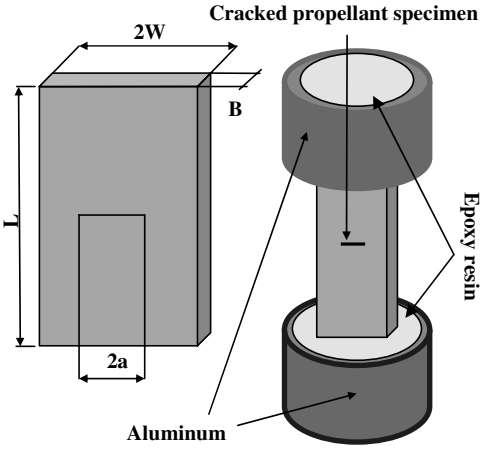

Fig. 2 Standard MT panel specimen geometry (cf. Table 1). The specimens were tabbed by embedding the ends in stiff epoxy resin and aluminum.

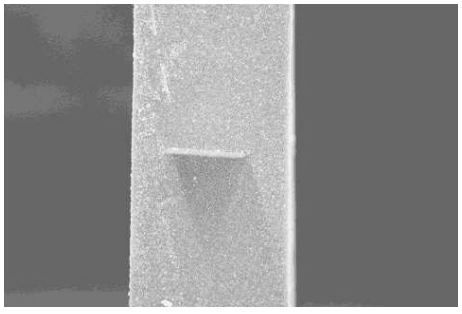

Fig. 3 Manually notching a crack in an MT specimen.

Data Analysis and Test Validity

With the data on the maximum load and the sample geometry, one can use the following exact solution [13] that is valid for the MT specimen to obtain K_{IC}:

$$K_I = \frac{P}{B\sqrt{W}} f\left(\frac{a}{W}\right) \tag{1}$$

where f is a geometric factor computed with the following expression:

$$f\left(\frac{a}{W}\right) = \sqrt{\frac{\pi a}{4W}\sec\frac{\pi a}{2W}}\left[1 - 0.025\left(\frac{a}{W}\right)^2 + 0.06\left(\frac{a}{W}\right)^4\right] \tag{2}$$

Compliance with the ASTM E399 [43] requires

$$B, a \geq 2.5\left(\frac{K_Q}{\sigma_{ys}}\right)^2 \tag{3a}$$

$$0.45 \leq a/W \geq 0.55 \tag{3b}$$

$$P_{\max} < 1.1P_Q \tag{3c}$$

In the standard, K_Q is a provisional toughness computed using the load P_Q obtained by intersecting the load-displacement curve with a line that has 95% of the initial stiffness. For filled elastomers, such as the propellant under investigation, a stiffness drop in a tensile test is not caused by plasticity, as with metals, but rather by the following two strain-energy dissipation mechanisms: viscous relaxation and damage due to the formation of microcracks (Fig. 4). Damage-induced softening [1,35] is irreversible and caused by cavitation (microcrack formation caused by dewetting of the filler particles or cohesive failure in the binder near the filler), which in turn is generated by disentanglements and relative displacements on a molecular scale, between chain segments of different lengths (which causes microfractures directly in the binder), or by direct scission of chain segments and strong bonds between binder and oxidizer. All damage mechanisms can be present with different shares, depending on test conditions (strain rate and temperature, which determine the available strain energy) and the properties of the individual compound (bonding agent effectiveness, plasticizer content, cross-link density, etc.). These irreversible-damage mechanisms are a

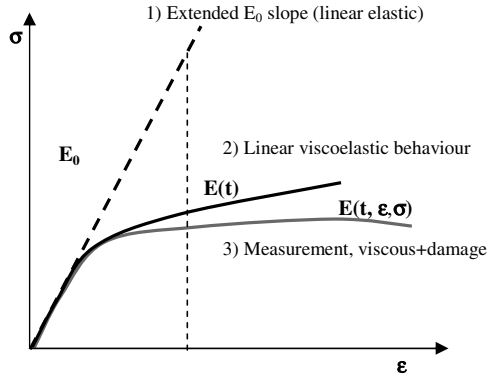

Fig. 4 Comparison of a linear–elastic, linear–viscoelastic, and nonlinear–viscoelastic response for a propellant subjected to a tensile test at constant displacement rate.

Table 2 Toughness-test results

Temp, °C	ε', mm/ min	K_{IC}, MPa · mm$^{1/2}$	SD,[a] %	Viscous dissipation,[b] %
20	50	1.72	4.3	Negligible
71	50	1.05	——	Negligible
−30	50	4.85	2.5	28
−30	2000	9.06	0.1	36

[a]Estimated standard deviation of the mean value.
[b]Difference between the secant stiffness at about 1% strain and the average stiffness computed using the LVE convolution between the time at 1% strain and rupture.

Table 3 Tensile tests at −30 and 71°C performed at different strain rates

Temp, °C	Strain rate, mm/min	Initial stiffness, MPa	Maximum stress, MPa
71	0.01	2.9	0.54
−30	50	15.8	2.1

source of linearity in the constitutive equation and therefore invalidate the assumptions of LEFM unless they are negligible because they are concentrated in a small process zone at the crack tip. Viscoelasticity, on the contrary, can be a linear (inelastic) characteristic of the material [13,44]. With Anderson ([13], chapter 8.1.3), because LEFM is valid for a linear–viscoelastic material as well as through the principle of correspondence [19], a test exhibiting more stiffness decay in the load-displacement curve than what is prescribed by the standard would still be valid if this decay was not due to large-scale yielding but to linear viscous relaxation. Therefore, if a stiffness drop caused by viscosity occurs, this does not invalidate the fundamental assumptions of LEFM and can be taken into account through the LVE material model. To do that, it is necessary to separate the contributions to the stiffness drop due to real damage and those due to the viscosity of the material.

A simple procedure is suggested: the instantaneous stiffness predicted by the LVE model is computed at the time for maximum load F_{max} and compared with the initial stiffness (Table 2). This is performed using the stress-relaxation modulus obtained during conventional testing (normally always available). Because the test is performed at a constant-strain rate, the strain is

$$\varepsilon(t) = \bar{\varepsilon}' \cdot t \tag{4}$$

Applying the LVE constitutive law for a constant-strain-rate test, one gets

$$\sigma(t) = \int_0^t E(t-\tau)\frac{\partial \varepsilon}{\partial \tau}\mathrm{d}\tau = \bar{\varepsilon}' \int_0^t E(t-\tau)\,\mathrm{d}\tau \tag{5}$$

using Eq. (4),

$$\sigma(t) = \bar{\varepsilon}' \int_0^t E(t-\tau)\,\mathrm{d}\tau = \frac{\varepsilon(t)}{t}\int_0^t E(t-\tau)\,\mathrm{d}\tau \tag{6}$$

The instantaneous slope is

$$\frac{\mathrm{d}\sigma(t)}{\mathrm{d}\varepsilon(t)} = E(t) = \frac{1}{t}\int_0^t E(t-\tau)\,\mathrm{d}\tau \tag{7}$$

substituting the Prony series in the Maxwell form [1] obtained by fitting the measured $E(t)$ curve, one obtains Eq. (8):

$$\frac{\mathrm{d}\sigma(t)}{\mathrm{d}\varepsilon(t)} = E(t) = \frac{1}{t}\int_0^t E(t-\tau)\,\mathrm{d}\tau = E_\infty + \frac{1}{t}\int_0^t \sum_{k=1}^{n} E_k e^{-\frac{t}{\tau k}} \tag{8}$$

where E_∞ is the rubbery modulus (i.e., the elastic part of the stiffness, which is characteristic of very slow loads applied at high temperature, without viscous contribution).

The equation shows that during a tensile test, a continuous stiffness drop occurs because of viscous relaxation. After a transient, the slope reached during such a test depends on the strain rate and the relaxation spectrum of the material. The viscous contribution to the stiffness drop can then be easily determined and used to compute an equivalent stiffness without viscous contribution, to find out whether the K_{IC} test is valid or not. The initial stiffness minus the viscous drop, and not 95% of the initial stiffness, as indicated in the E399 standard, is then used to compute P_Q. If viscous dissipation, and not true damage, produces the largest stiffness drop in a specific test, the computed P_Q value will be higher than that obtained from the 95% initial stiffness prescribed by the standard and therefore nearer to P_{max} (cf. Fig. 5). If a master curve for the stress-relaxation modulus in tension is not available, one can perform a direct relaxation test under the same conditions of the K_{IC} test to assess the stiffness drop caused by viscosity, as was done by Bencher et al. [28].

Example

An example of the preceding methodology is given for a K_{IC} test performed at −30°C and a strain rate of 50 mm/ min. Note that results from the uniaxial tensile test to failure performed at two different temperatures and strain rates indicate that viscoelastic effects are indeed relevant: at −30°C and 50 mm/ min, the material builds up a large viscous stress component (cf. Table 3). At this temperature, relaxation is much slower than at 71°C and plays a fundamental role with respect to the failure stress. The initial stiffness is also considerably higher.

The table and the simulation in Fig. 6 show that the drop of stiffness is not negligible at −30°C and 50 mm/ min, whereas at 71°C and slow-to-moderate strain rates, the drop of stiffness is negligible and $E(t) \approx E_\infty$ (Fig. 7). In the test, the maximum load before failure is 253 N at a displacement corresponding to a strain of 8.1% (Fig. 8).

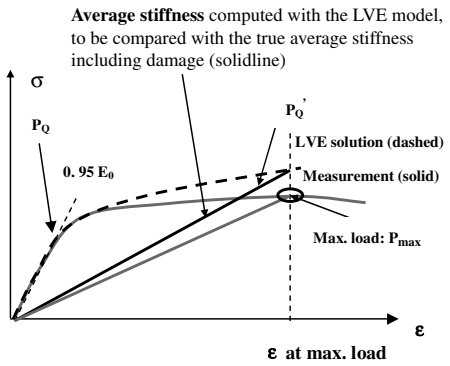

P_Q – Maximum load in a tensile test computed for with the LVE material model at the displacement corresponding to the maximum measured load
P_Q' – Maximum load in a tensile test computed using "95% of the initial stiffness"
P_{max} – Maximum measured load

Fig. 5 Toughness-test validity check separating viscoelasticity from real damage.

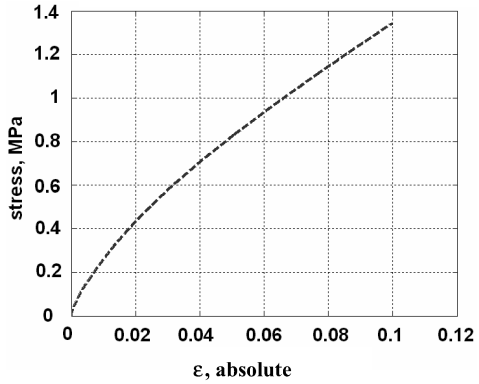

Fig. 6 Simulated tensile test at $T = -30°C$ and 50 mm/min strain rate with the LVE material model shows the stiffness decrease caused by viscous relaxation.

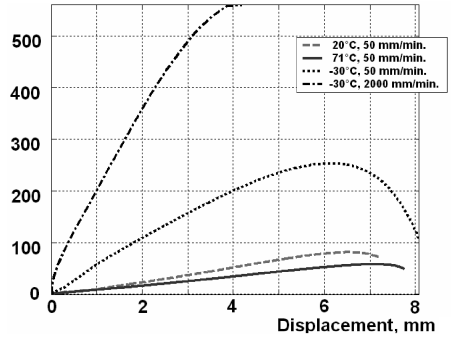

Fig. 7 Load-displacements plots from K_{IC} tests.

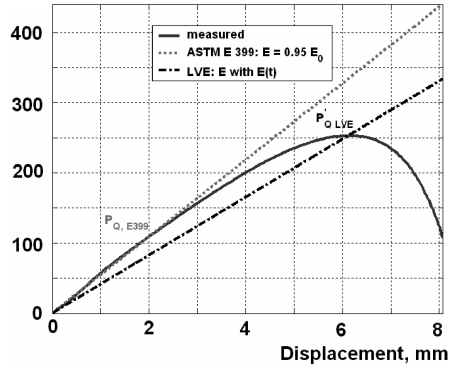

Fig. 8 Application of the proposed data analysis method and the original ASTM E399 procedure to a toughness test at −30°C and 50 mm/min.

Applying the ASTM E399 standard method to the test, the initial stiffness is readily calculated by collocating a least-squares slope at the beginning of the stress–strain plot: at low strain (2%) we obtain 31.2 MPa with a correlation factor $R^2 = 0.999$. Calculating the prescribed 95% slope, one obtains 29.7 MPa and plots it in the graph, to find that the intersection load P_Q computed with the ASTM E399 methodology is much lower than 0.9 of the maximum measured load, which is the validity limit prescribed by the norm. One would then conclude that the test is invalid, and because the source of the stiffness drop would be erroneously interpreted as plasticity or damage, the conclusion would be that the material experiences plastic/damage effects not only at the crack tip, but also in most of the specimen, invalidating LEFM assumptions.

Applying the methodology outlined before, one can instead separate the viscous stiffness drop from the drop due to real damage using the stress-relaxation modulus $E(t)$, available from the standard LVE characterization. It is therefore easy to compute the intrinsic stiffness decay due to viscosity by applying the LVE material model to this test [Eq. (8) and Fig. 6].

In the test, the maximum load is reached after 7.75 s. At this time and test conditions, the average stiffness according to the LVE material model is 72% of the initial value. By assumption, this stiffness drop is entirely caused by viscous dissipation. As a matter of fact, from previous tensile testing, one knows that 8% strain is fully recovered and does not damage the propellant: the damage region due to microcrack formation [35] starts at strains above 15% at −30°C and 50 mm/min. LEFM is then applicable [19] and one can calculate a new slope by applying a factor of 0.72 to the initial stiffness, obtaining 22.5 MPa. Plotting this slope, one can observe that the intersection with the measured test curve P'_Q is almost at the maximum load (Fig. 8). The minimum load for validity according to the standard is 227.6 N (5% true damage), which is below the value obtained separating viscoelasticity and applying the ASTM factor of 0.95 (i.e., 244 N). The test is therefore valid and gives a K_{IC} of 4.76 MPa · mm$^{0.5}$.

Results

The toughness-test results are summarized in Table 2. Dependence of the toughness on the geometry of the specimen was checked by testing different geometries: MT-1 and MT-2 (cf. Table 1). Results are shown in Table 4. Although for some materials, due to the size effect, a larger specimen gives a lower toughness [45], for high-toughness medium-elongation propellants, it seems to be the contrary [30,45]. The difference between plane-stress and plane-strain conditions would generate a maximum critical stress-intensity-factor deviation of $(1 - \nu^2)^{-(1/2)}$ (i.e., 0.87 for the thicker specimen if the material is incompressible). The reason for the moderate geometry dependence is not clear at the moment and would require further investigation; it limits the validity of a LEFM approach for a full grain using failure data from subscale specimens and justifies the NLFM testing approach.

An overview of typical displacement-load curves obtained during the tests is reported in Fig. 7; they show the significant difference in the work required to propagate a fracture at different strain-rate/temperature combinations.

Toughness Data Correlation

At high temperature, the relaxation processes in the propellant are accelerated. Therefore, the effect of energy dissipation by viscoelasticity on a tensile test is not observed if the strain rate is very slow and/or the temperature is high; damage effects on a microscopic scale occur in a very small zone at the crack tip: one would therefore measure an essentially constant-slope stress–strain curve, with the slope being about E_∞. This means that a viscoelastic material in which fracture propagation occurs in a very long time and/or at high temperatures would not benefit significantly from viscous dissipation (reducing the available energy to propagate the crack), and the K_{IC} values extracted from the test reach a lower, limiting, value. If the load is applied with a higher strain rate and/or at lower temperatures, so that the time scale of the test is smaller than the time required to reach complete relaxation, then some strain energy is lost by viscoelasticity. This dissipation mechanism increases the effective toughness of the material.

Toughness data can therefore be correlated as conventional failure properties using the temperature reduced strain rate [46]. Tests at different temperature and strain rate with the same $\varepsilon' \cdot a_T$ value produce equal toughness results: the reduced strain rate can be used as a characteristic number for thermoviscoelastic similitude. A master curve for the toughness is thus obtained (Fig. 9a). The

Table 4 Two toughness results using different specimen's geometries

T, °C	ε', mm/min	Geometry	K_{IC}, MPa · mm$^{1/2}$
20	50	MT-2	1.43
20	50	MT-1	1.67

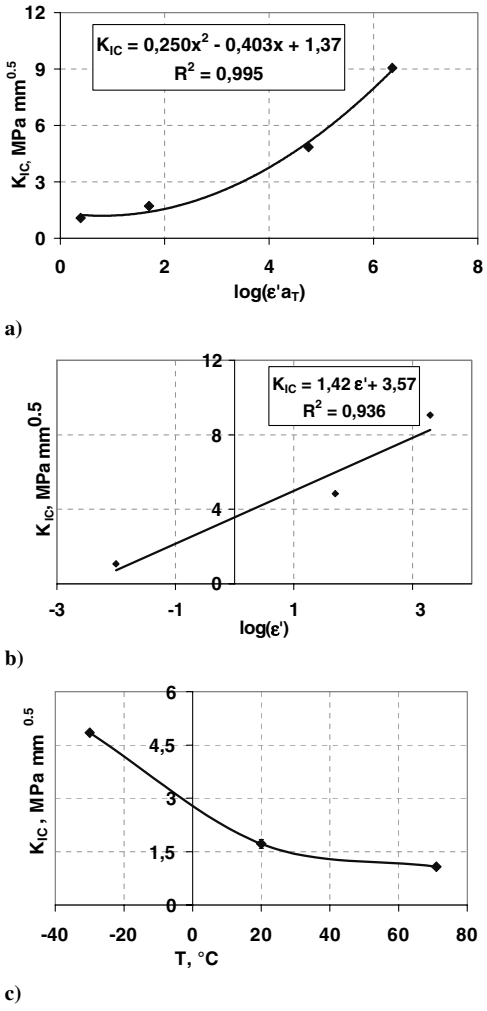

Fig. 9 Plots of a) master curve for K_{IC} (strain rate in mm/min), b) K_{IC} dependence on strain rate, and c) K_{IC} dependence on temperature.

separate influences of material temperature and strain rate are shown in Figs. 9b and 9c.

Comments

Results are found to be consistent with Knauss's [18] and Shapery's [19–21] theories. Its application to the tests lead to the formulation of a correlation that allows the computation of the toughness at different test conditions using reference test results. Furthermore, some of the features described in the papers by Liu [30] and Bencher et al. [28] were analyzed and explained.

First, we consider a constant-strain test on a MT specimen. The FPZ fails when the material reaches a critical strain ε_{cr} close to or proportional to the rupture strain of the pure binder (Fig. 10), which is of the order of 100–200%:

$$\varepsilon(t) = \bar{\varepsilon}' t \Rightarrow \varepsilon_{cr} = \bar{\varepsilon}' t_{cr} \tag{9}$$

The local stress in the FPZ is assumed to be equal to the crazing stress for the propellant, σ_{cr}, because the material has a rather flat stress–strain curve after the onset of softening. Failing of the FPZ is simply a matter of time under load because the FPZ material creeps, being viscoelastic (a stress threshold does, however, exist because of cross links in the binder and the strong bonds between AP and binder generated by the bonding agent). Applying the principle of correspondence, one can estimate an equivalent stiffness from $t = 0$ to the time to failure t_{cr} and neglect the elastic part of the stiffness (accurate only if the temperature is not too high and the strain rate is not too low in the FPZ). With

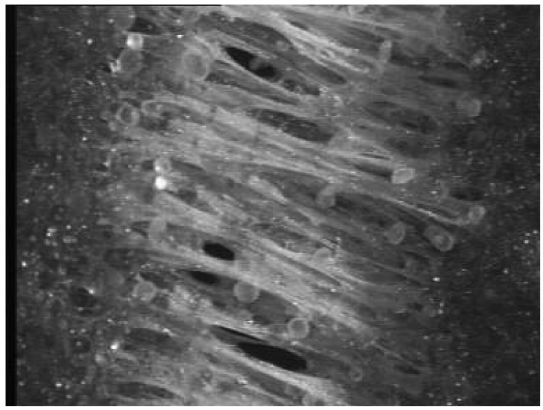

Fig. 10 FPZ in the propellant.

$$E(t) = E_\infty + E_1 t^{-n} \tag{10}$$

a best fit for the material gives $E_1 = 6.93$ MPa and $n = 0.20167$; then

$$\sigma_{cr} = \varepsilon_{cr} E_1 t_{cr}^{-n} = \varepsilon_{cr} E_1 \left(\frac{\varepsilon_{cr}}{\bar{\varepsilon}'}\right)^{-n} \tag{11}$$

Within LEFM, the stress intensity factor is proportional to the stress [12]:

$$K_{IC} \propto \sigma_{cr} = \varepsilon_{cr} E_1 \left(\frac{\varepsilon_{cr}}{\bar{\varepsilon}'}\right)^{-n} \Rightarrow K_{IC} \propto \varepsilon_{cr} E_1 \left(\frac{\bar{\varepsilon}'}{\varepsilon_{cr}}\right)^{n} \tag{12}$$

The toughness would therefore be proportional to the strain rate to the power n. The following correlation is obtained at different strain rates:

$$\frac{K_{IC}|_{\bar{\varepsilon}'_2}}{K_{IC}|_{\bar{\varepsilon}'_1}} = \left(\frac{\bar{\varepsilon}'_2}{\bar{\varepsilon}'_1}\right)^{n=0.20167} \tag{13}$$

At $T = -30°C$ one would predict

$$\frac{K_{IC}|_{2000\ \text{mm/min}}}{K_{IC}|_{50\ \text{mm/min}}} = \left(\frac{2000}{50}\right)^{n=0.20167} = 2.1$$

Checking the prediction with experimental data,

$$\frac{K_{IC2000}}{K_{IC50}} = \frac{9.062}{4.846} = 1.9$$

This is indeed close to the prediction. The dependence on strain rate is rather small, in agreement with the fact that the speed of stress relaxation for HTPB propellants is more sensitive to temperature than the strain rate between glass transition and the rubbery region. Liu [30] obtained similar toughness values, and the values reported by Bencher et al. [28] are also of the same order of magnitude; considering the value of the exponent n and the strain-rate range investigated, it is therefore not surprising that both report a more moderate dependence on the strain rate than on temperature.

Acceleration of the Crack Speed During a Test

Applying Shapery's theory, one can also explain why a progressive acceleration of the crack-propagation speed was observed during the tests and why the crack-propagation speed was higher at lower temperatures and strain rates. The speed of crack propagation for a material with a constant fracture energy Γ and a constant length of the FPZ (α) follows:

$$a'^n \propto J_v \tag{14a}$$

Assuming linearity,

$$a' \propto K_I^{2/n} \tag{14}$$

where $2/n = 10$ for this propellant. Because K_I increases during the test as the crack size increases, there is a remarkable acceleration of the crack until failure, as was indeed observed from video recordings of the tests.

Crack-Growth-Resistance Curves

Crack-growth-resistance curves were published by Liu [8,30] in terms of K_I vs Δa and by Bencher et al. [28] as J_v vs Δa. The propellant can be considered as linear, except inside the FPZ, so that the two curves are related through following equation [13,20,21]:

$$J_v = \frac{K_I^2(1-\nu^2)}{E_R} \tag{15}$$

The particular shape of crack-growth-resistance curves can then be inferred directly from the power- law relationship for the crack speed:

$$a' = kG^{\alpha} \tag{16}$$

One of the fundamental results of Shapery's theory (cf. [42]) is the prediction of the exponent a depending on the nature of the FPZ and the creep compliance of the material in the FPZ. If the process zone has a constant size, then $\alpha = 1/n$, where n is the exponent in the power-law expression for the relaxation modulus [Eq. (10)] (here, $n = 0.2$, and therefore $\alpha = 5$):

$$a' \propto J_v^{1/n} / a' \propto K_I^{2/n} \tag{17}$$

Integrating in time,

$$\int_0^t a' \, \mathrm{d}t \propto \int_0^t J_v^{1/n} \mathrm{d}t$$

Therefore,

$$\Delta a^n \propto \left[\int_0^t J_v^{1/n} \mathrm{d}t\right]^n = L_{1/n}\{J_v\} = L_{\alpha}\{J_v\} \tag{18}$$

where Δa is the crack extension during the load history between $t = 0$ and t; t is the time or material time (reduced time), taking temperature and even aging into account; and $L_n(J_v)$ the Lebesgue norm of J_v during the cycle ($1/n$th order). For $n \to 0$ the Lebesgue norm of $1/n$ is the norm of the supremum. Only the maximum value of J_v is reached during the load counts; otherwise, there is an amount of crack extension before the maximum load is reached:

$$L_{\infty}\{J_v\} = \lim_{n\to 0}\left[\int_0^t J_v^{1/n} \mathrm{d}t\right]^n = \sup_{0-\bar{t}}\{J_v\} \tag{19}$$

This is consistent with a linear time-independent behavior, such as the Mullins effect.

Considering the shape crack-growth-resistance curves shown by Liu [8,30] and Bencher et al. [28], a power-law dependence of J_v or K_I on Δa of qualitatively the same shape is predicted. A material with $n = 0.2$ and a constant-process-zone size $\alpha = 1/n$ (here, $\alpha = 5$) will have a rather steep transition between the region of stable propagation and instability [13]. Moreover, the transition of the curves should become sharper with higher temperature and lower strain rate, because n decreases and the material relaxes so fast that it can be considered to be almost time-independent ($n \to 0$). This is consistent with the data provided by Liu [8,30] and Bencher et al. [28].

Liu [8,30] reports that the crack-resistance curves can be separated into 3 regions. In region I, between zero and a threshold K_{Ic}, no crack advancement occurs. A second region follows, characterized by stable crack growth: after an initial crack propagation by Δa when $K_I > K_{\mathrm{Ic}}$, a further increment in load is required for further propagation. This behavior is typical of materials with a FPZ characterized by cohesive stresses. In zone I, the load can be absorbed by the elastic part of the stiffness E_{∞} in the FPZ, and the speed of crack propagation goes to zero. The material has the intrinsic ability to elastically support some loads without creep because of cross links [19,20], entanglements, and the effect of the bonding agent. Several effects can explain a region II behavior for the propellant. First, the material ahead of the FPZ is certainly strained to some extent in the load direction; this means that some orientation of the molecular segments occurs each time the material is loaded, and this way, once the new FPZ is formed, it will require higher stresses to be destroyed because of a higher density of molecular chain segments bridging the FPZ. Also, the highly stretched binder segments enter a strain range in which the end-to-end distance follows Langevin statistics: in this strain range, there is an upcurl in the stress–strain curve [47]. Region III is a region of instability: a constant K_I produces an indefinite crack extension, and the crack proceeds with an increasing speed [Eq. (14)]. The toughness results obtained here are values of K_I at the onset of instability (i.e., at the limit between regions 2 and 3 of a crack-resistance curve).

Shapery [26] and Liu [30] report that the propagation is not continuous: a FPZ is formed, the FPZ is destroyed by the load, and a new FPZ must be generated before further advancement. Region II behavior and discontinuous growth with steps equal to a FPZ size are also typical of other composite materials with hard particles, such as concrete [34]. This justifies the application of NLFM models and tests developed for cementitious materials in the field of civil engineering to composite solid propellants. Anticipating the results of WST tests for NLFM characterization, the peak load in a test is always reached when the FPZ is indeed fully formed and starts to collapse.

Blunting and Crack-Opening Displacement, FPZ Sizes, and Process-Zone Morphologies

An estimate of the FPZ size can be performed applying either Shapery's theory or Dugdale's model. Applying the latter, formulas for the length of the FPZ and the crack-opening displacement (COD) [13] can be applied to investigate their dependence on temperature and strain rate:

$$\rho_c = \frac{\pi}{8}\left(\frac{K_{\mathrm{IC}}}{\sigma_{\mathrm{cr}}}\right)^2 \tag{20a}$$

$$\delta_c = \frac{K_{\mathrm{IC}}^2}{\sigma_{\mathrm{cr}} E(t_\rho)} \tag{20b}$$

$$t_\rho = \frac{\rho_c}{a'} \tag{20c}$$

where ρ_c is the length of the damage zone from where the stress is zero to the crack tip, σ_{cr} is the crazing stress for the material, and t_ρ is the time required by the crack to propagate with speed a' by a length equal to ρ_c. Using the K_{IC} measurements and the standard characterization results, the following values are obtained (Table 5).

Results are consistent with visual observations during testing. At lower temperature and/or lower strain rate, both the COD and the length of the FPZ increase; the failure stress increases significantly, as pointed out in the standard characterization section. The fracture energy increases as well, because the strain capability for a HTPB-based solid propellant increases before dropping sharply in the proximity of glass transition (Fig. 3). Therefore, the fracture toughness of the material follows the trend of the bulk fracture

Table 5 FPZ size predicted with the Dugdale–Barenblatt theory

T, °C	Max. stress, MPa	K_{IC}, MPa · $\mathrm{mm}^{1/2}$	FPZ size, mm
71/50 $\mathrm{mm/min^{-1}}$	0.9	1.06	0.54
20/50 $\mathrm{mm/min^{-1}}$	1.35	1.72	0.64
−30/50 $\mathrm{mm/min^{-1}}$	2.42	4.85	1.56
−30/2000 $\mathrm{mm/min^{-1}}$	3.59	9.06	2.51

energy: it is low at high temperatures and slow strain rates, when the fracture proceeds mostly in the binder by disentanglements and suppression of weak van der Waals bonds, and it increases when the relaxation processes slow down, at lower temperature. At these conditions, the failure stress increases by an order of magnitude and the strain increases too, reaching a peak; the fracture proceeds by destruction of strong bonds at the bonding agent or in the binder and requires a maximum of energy (Fig. 10).

After the strain drops sharply across glass transition, the fracture energy drops and the fracture proceeds by direct chain scission of the molecular segments randomly oriented in the direction of the load in a very small region close to the crack tip. In the FPZ, the fracture energy is then related to the density of cross links, the effectiveness of the bonding agent, and, globally, to the number and toughness of crazing filaments at the crack tip [28].

Wedge-Splitting Tests: Fracture Energy, Fracture Toughness, and Calibration of the NLFM Model

The matrix of composite solid propellants is a binder (typically a polyurethane) enriched by plasticizer. A crack in a composite solid propellant is characterized by entangled binder filaments bridging the crack. Bonding agent molecules anchor the binder filaments to the oxidizer particles with strong bonds and confer higher toughness to the material, increasing crack bridging (Figs. 13 and 14). Hence, along a portion of the crack, there is a transfer of stress through the stretched binder, giving rise to a FPZ along which there is a distribution of cohesive stresses.

A model for cohesive stresses at the tip of a crack for cementitious material (such as concrete, a composite material made of a cement matrix and aggregate inclusions) was first proposed by Hillerborg et al. [48]. This very simple and elegant model, which is an extension of those of Dugdale [22] and Barenblatt [23], decomposes the crack into two parts (Fig. 12):

1) There is a true or physical crack across which no stresses can be transmitted. Along this zone there is both a displacement and a stress discontinuity.

2) There is a fictitious crack, or FPZ, ahead of the previous one, characterized by the a peak stress at its tip equal to the tensile strength of the material and a decreasing stress distribution from f'_t ($s_{\max}$) at the tip of the fictitious crack to zero at the tip of the physical crack. The area under the softening curve is the fracture energy G_F (i.e., the energy needed to extend the crack by a unit length).

Looking at Figs. 10 and 11, the assumptions of the model seem coherent with the FPZ morphology of composite propellants. It should be noted that along the FPZ, there is displacement and strain discontinuity and stress continuity. Finally, it should be noted that whereas in LEFM, the energy is dissipated entirely along the crack tip (characterized by the critical energy release rate $G = K_{IC}^2/E'$), in NLFM, the energy is dissipated along the fracture process zone.

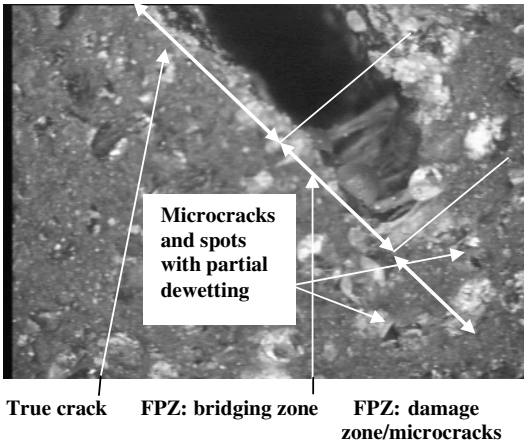

Fig. 11 FPZ in a propellant with a similar formulation. This picture was taken at 20°C; the FPZ morphology is identical to that of the propellant tested in this work (Fig. 10).

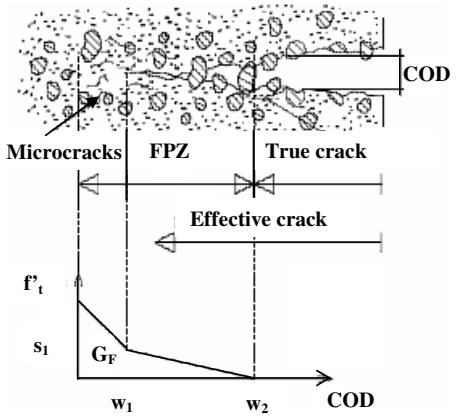

Fig. 12 Hillerborg et al.'s [48] fictitious crack model.

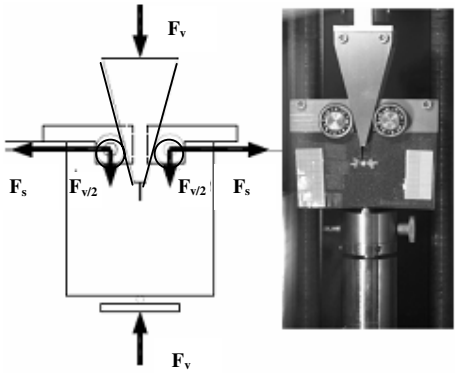

Fig. 13 WST setup and acting forces (left) and WST propellant specimen ready for a test (right).

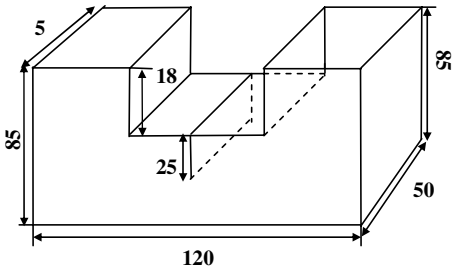

Fig. 14 Nominal dimensions of the specimens for the WSP (all dimensions in millimeters).

In theory, if the size of the FPZ is negligible compared with the total crack length, then $G = G_F$. It has been shown that in the presence of a negligible FPZ size (as is usually the case for concrete), linear–elastic fracture mechanics is incorrect, and a NLFM approach should be followed instead.

Finally, because energy is released from a volume to create a surface energy, this length discrepancy (from L^3 to L^2) gives rise to a size effect as originally shown (through energy transfer considerations) by Bažant [49] or, more recently (through the zeroing of the stress intensity factors), by Saouma et al. [45]. This model is now universally accepted in the concrete community and has also been used in ceramics [50] and rocks.

Wedge-Splitting Test

Whereas most standard fracture-mechanical tests have a relatively low ratio of fracture ligament length over volume of material (and indeed a short crack too), the wedge-splitting test is an effective alternative to those tests, allowing the direct determination of some material parameters necessary to NLFM models. The test method

introduces a controlled lateral opening displacement through a wedge, inducing stable crack growth in a prismatic or cylindrical specimen (Fig. 13). It provides a mean of measuring the resistance to crack propagation using LEFM (K_{Ic}) or NLFM (G_F) models. From the splitting force-average crack-opening displacement response of the specimen, the specific fracture energy is determined. For fracture-toughness evaluation, a series of unload–reload tests is necessary.

Results may be used in numerical simulations based on LEFM or NLFM as well as in comparative studies of the fracture properties of different materials. This has been done with rocks for civil engineering purposes, for instance, and is now applied to solid propellants.

Testing Procedure

The testing system consists of frame, actuator, force cell, controller, and data acquisition equipment at a minimum. Whereas it is preferable to have a closed-loop servo-controlled machine, this is not essential for solid propellants because of their low stiffness and their intrinsic capability to dissipate excess energy through viscosity. A climatic chamber on the tensile machine is essential to measure the propellant properties in the temperature range specified for the rocket motor.

The specimen size used during this study is shown in Fig. 14. If possible, the specimen size should be chosen in such a way to be representative of the grain size (e.g., the web thickness for radial cracks), to compensate for size effects, which are not explicitly taken into account by this methodology.

The test procedure adopted for this test series is now described. The machine worked under stroke control, in compression, applying a vertical force on the wedge; the chosen temperature and stroke (crosshead) displacement rate in compression were set before the test to be representative for the load case. Test conditions for all propellant specimens were varied to obtain a master curve of properties and are reported in Table 6 with the test results. For a brittle and stiff material such as concrete, the rate is necessarily low (e.g., 0.2 mm/ min). Temperature conditioning time for the WST specimens was at least 12 h, to obtain a uniform temperature in the material. The specimen was left in the climate chamber of the tensile machine for 10 min before starting the test. For a fracture-toughness test, the application of one unload/reload close to the force peak at the same rate of the first loading is required (cf. Fig. 15 for a typical load-displacement plot); this procedure needs to be repeated at least 4 times in the postpeak zone.

The following quantities are measured during each test: the vertical force F_V and vertical displacement ΔV as a function of time, the crack-opening displacement at the beginning of the FPZ (using a Vic2-D Limess image correlation extensometer), and the displacement field at the crack (this is optional, but can be used for a simulation of the test and inverse analysis on a 2-D displacement field).

Data Analysis

Fracture Toughness

The determination of the fracture toughness K_{Ic} requires not only the maximum load, but also the corresponding crack size. The procedure to determine the LEFM toughness from unload–reload data is not reported here and is described in [33]. It is just observed that in propellants, as in rock and concrete, the tip of the crack may not be easily identifiable due to the heterogeneity introduced by the oxidizer grains. Hence, to determine the fracture toughness, the concept of an elastic equivalent crack length has to be applied, and the latter is determined through the compliance method, which combines finite element calibration of the test and analysis of experimental data, giving better results than the MT specimens for conditions at which the FPZ length/size is not negligible (low-to-intermediate temperatures and high rates).

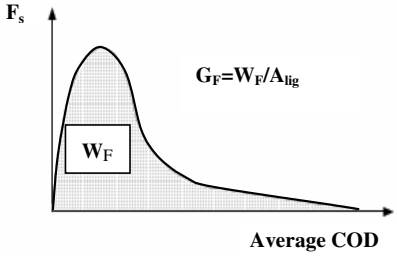

Fig. 15 Definition of work of fracture and specific fracture energy.

Fracture Energy

The following steps are needed to determine the fracture energy:

1) Determine the (horizontal) splitting force acting on the roller bearing F_S from

$$F_s = \frac{1}{2\tan\alpha} F_V \tag{21}$$

(for the propellant, a wedge half-angle of 30 deg was used).

2) Determine the lateral displacement induced by the wedge or, if possible, the average of the displacements induced on both sides of the specimen. Otherwise, determine the crack-mouth-opening displacement (CMOD) induced by the wedge or the average of the CMODs on both sides.

3) Plot F_S in terms of CMOD and, if necessary, extrapolate the force-displacement curve to zero F_S. Extrapolation is required if the two split parts of the specimen reach the support and this happens at an appreciable force.

4) Determine the ligament area A_{lig} corresponding to the projected area of the crack on the ligament by examining the sample after the test and/or by measuring the individual sample geometry before the test.

5) Determine the work of fracture W_F as the area under the F_S-COD curve (Fig. 15) by numerical integration.

6) Determine the specific fracture energy with

$$G_F = W_F / A_{lig} \tag{22}$$

Analyze the test images at the peak of the force curve or after the peak, during propagation, and determine the critical COD at the end of the true crack, where the FPZ begins, together with the time at which the force peak is reached. The force peak was reached at the

Table 6 WST test results

Test no.	T,°C	a_T	Displacement rate, mm/ min	$\log(a_T\text{-COD}')$	G_F, mJ/mm^2	Average	SD, %
WST 6	20	1	57.74	−1.3	1.87	1.98	7.7
WST 7	20	1	57.74	−1.3	2.09	——	——
WST 8	−20	1.43×10^2	115.47	1.07	9.80	9.96	2.3
WST 9	−20	1.43×10^2	115.47	1.07	10.12	——	——
WST 10	−40	1.56×10^4	115.47	2.84	21.40	20.9	3.6
WST 11	−40	1.56×10^4	115.47	2.87	20.32	——	——
WST 12	−60	8.91×10^7	577.35	8.88	14.24	14.9	6.1
WST 13	−60	8.91×10^7	577.35	8.88	15.52	——	——
WST 14	71	4.51×10^2	5.77	−3.99	0.49	0.51	6.6
WST 15	71	4.51×10^2	5.77	−3.94	0.53	——	——

onset of propagation, where the FPZ is fully formed. This means that the energy applied by the machine between the beginning of the test and the force peak is the energy required to form the FPZ, including viscous dissipation. This last operation is necessary to obtain a fracture-energy master curve for the propellant and would be necessary for any filled or unfilled elastomer or plastic showing time and temperature dependence. The critical COD is itself a material property representative of the toughness, proportional to the critical value of the J integral at which propagation occurs [13]. A G_F master curve should report the rate of COD times the temperature factor in the abscissa, because the material's failure properties depend on the reduced strain rate and, during a load history in a SRM (or another structure), the material in the FPZ is stretched differently in the bulk and at the FPZ until the critical COD value is reached (i.e., until local collapse and propagation of the FPZ zone in the grain occur).

Indeed, looking at Fig. 10, one can easily realize that the strain of the binder filaments in the FPZ can be of the order of 100–200% and is applied within *the same* loading rate of the bulk. As a consequence, the strain rate in the FPZ is completely different from that for the rest of the propellant. Moreover, because the critical COD is a material property itself, the same critical COD value will be reached inside a motor if a crack is propagating.

Therefore, the determination of the G_F from a G_F master curve for the purpose of simulating a load case should be done using the appropriate temperature factor a_T combined with the rate at which the critical COD is reached [i.e., dividing the critical COD with the loading time (for instance, the time from firing of the igniter until the peak pressure in the motor is reached)].

Test Results

Test results are summarized in Table 6. All tests mentioned in this work were performed on a Zwick tensile machine certified to class 0.5 according to standard DIN EN ISO 7500-1. Calibration showed a minimum accuracy of 0.2% in the measured force range, which gives negligible errors in terms of G_F. Temperature-setting precision is ±2°C. Within glass transition, in which temperature sensitivity is high, this generates an accuracy of about 0.5 in terms of log(COD′a_T) (see the abscissa in Figs. 16 and 17). Pictures of the FPZ from the WST tests are shown for all tested conditions (Figs. 18a and 18b). Note that as predicted, the sizes of the FPZ and the COD increase from warm to cold and with the stroke rate. Between −40°C and 100 mm/ min stroke rate and −60°C and 500 mm/ min, glass

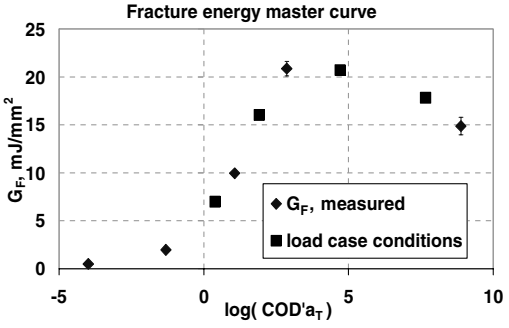

Fig. 16 G_F master curve. Diamonds are the averages of the values reported in Table 6. Error bars indicate ± the standard deviation.

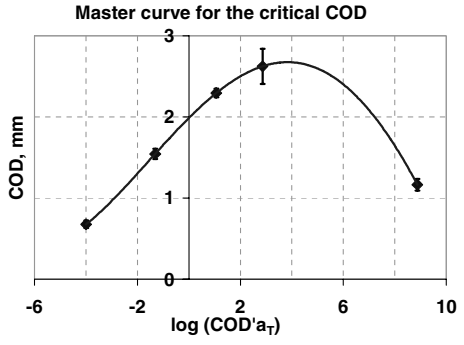

Fig. 17 Master curve for the critical COD. Note the drop in COD in correspondence with the onset of glass transition. Error bars indicate ± the standard deviation.

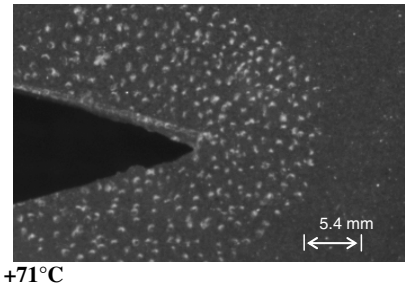

+71°C

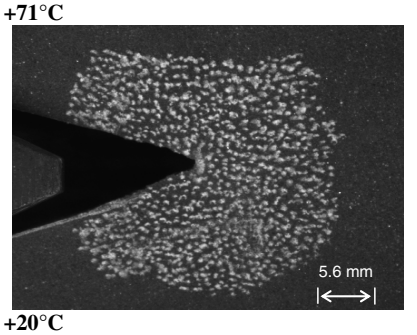

+20°C

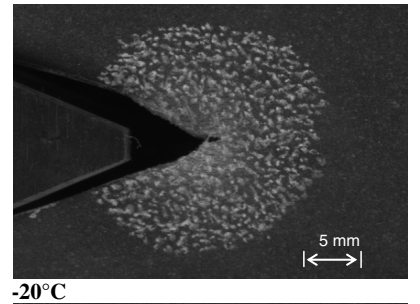

-20°C

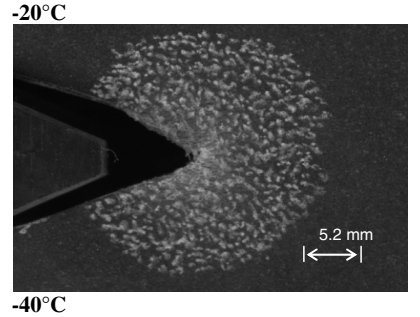

-40°C

a)

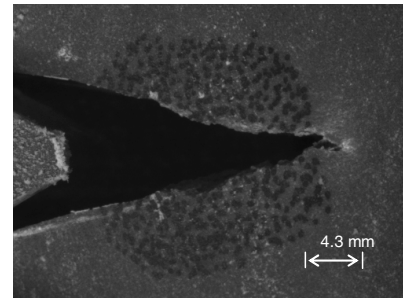

-60°C

b)

Fig. 18 FPZ a) and COD between 71 and −40°C (at 71°C, the fracture easily proceeds in the very soft binder and propagation requires little energy) and b) at −60°C shows the onset of ductile to brittle transition in correspondence with the onset of glass transition (sharp crack tip).

Table 7 Material properties for the NLFM analysis

Load	T,°C	a_T	$\log(a_T\text{-COD}')$	G_F, mJ/mm^2
Ignition	71	3.51×10^2	0.07	2.08
Ignition	20	1	1.82	7.72
Ignition	−30	5.83×10^2	4.59	20.9
Ignition	−50	7.65×10^5	7.41	19.7

transition begins, making the material more brittle. The master curves for fracture energy G_F and the critical COD are shown in Figs. 16 and 17. The shape of the curves is similar, in accordance with theory. Also, glass transition causes a drop of more than 25% in G_F and is not complete at −60°C and 500 mm/ min. The embrittlement of this propellant is typical of similar formulations and is far more gradual than that observed with homogeneous double-base propellants. The squares in Fig. 16 indicate the G_F values calculated for the load cases to be subjected to finite element analysis and have been obtained by interpolating the measurements with a piecewise cubic Hermite polynomial. The corresponding rate of COD has been calculated by dividing the critical crack-opening displacement obtained from the COD master curve (Fig. 17) for the load-case conditions by the duration of the pressurization ramp. The values are reported in Table 7.

Conclusions

A fast-burning AP-HTPB-based solid propellant has been tested by applying both standard and fracture-mechanical test methods to determine the critical crack size for a motor at ignition through finite element analysis implementing LEFM and NLFM techniques. A master curve for the fracture toughness has been obtained using MT specimens. Test results have been compared with those previously reported by other researchers and proved to be consistent with Shapery's theory.

Nonlinear fracture-mechanical characterization was carried out using the WST test technique, originally developed for cementitious materials and rocks; after some adaptations, the WST methodology proved to be applicable to the propellant and gave reproducible results in line with expectations, allowing a direct determination of the material parameters required for NLFM simulation of a motor with bore cracks.

Master curves for the fracture energy G_F and the critical COD have been obtained. The material propensity to subcritical and critical crack propagation has an essential effect on the safety and performance of a SRM design, as it can determine the ultimate failure condition of the motor and/or the motor's shelf life. Because of that, the measurement of fracture energy through WST testing is recommended as an effective way to complete the mechanical characterization methods that are usually applied to composite propellants during development and production.

When failure scenarios associated with cohesive crack propagation in a grain are being considered, the WST test is, in our opinion, an essential tool to determine the relevant mechanical properties of any formulation.

Acknowledgments

The authors would like to thank MBDA Bayern-Chemie, GmbH, for its support of this experimental test programme, particularly D. Gulden and K. Schmid and the manufacturing team for the skill and flexibility shown in preparing new samples. The help of Jim and Kathy Buswell during the revision of this paper is gratefully acknowledged.

References

[1] "Solid Propellant Grain Structural Integrity Analysis," NASA Rept. SP-8073, June 1973.

[2] "Structural Assessment of Solid Propellant Grains," AGARD Rept. AR 350, Neuilly-sur-Seine, France, Dec. 1997.

[3] Francis, E. C., and Carlton, C. H., "Some Aspects of Composite Propellant Nonlinear Behavior in Structural Applications," *Journal of Spacecraft and Rockets*, Vol. 6, No. 1, 1969, pp. 65–69.

[4] Mullins, L., "Softening of Rubber by Deformation," *Rubber Chemistry and Technology*, Vol. 42, No. 1, 1969, pp. 339–362.

[5] Reeling Brouwer, G., Weterings, F. P., and Keizers, H. L. J., "Evaluation of Aging in Composite Propellant Grains," 41st AIAA Joint Propulsion Conference, AIAA Paper 2005-3803, July 2005.

[6] Fitzgerald, J. E., and Hufferd, W. L., "Handbook for the Engineering Structural Analysis of Solid Propellants," Chemical Propulsion Information Agency Publ. 214, Columbia, MD, May 1971.

[7] Liu, C. T., "Fracture Mechanics and Service Life Prediction Research," U.S. Air Force Research Lab. TR PR-ED-AB-2002-208, Propulsion Directorate West, Edwards AFB, CA, 2002.

[8] Liu, C. T., "Crack Growth Behavior in a Composite Propellant with Strain Gradients Part 2," *Journal of Spacecraft and Rockets*, Vol. 27, No. 6, Nov.–Dec. 1990, pp. 647–652.

[9] Little, R. R., Chelner, H., and Buswell, H. J., "Development, Testing and Application of Embedded Sensors for Solid Rocket Motor Health Monitoring," 37th International Annual Conference of ICT, Fraunhofer Inst. fur Chemische Technologie, Paper 21-1, June 2006.

[10] Neely, R. B., and Veit, P. W., "Solid Rocket Motor Grain Design Verification Through Cold Gas Pressurization and Motor Dissection," AIAA Paper 74-1202, Oct. 1974.

[11] Buswell, H. J., "Lessons Learned from Health Monitoring of Rocket Motors," 41st Joint Propulsion Conference, AIAA Paper 2005-4558, July 2005.

[12] Liu, C. T., "The Application of Fracture Mechanics to Predict the Critical Initial Crack Length," U.S. Air Force Research Lab. TR PR-ED-TP-2003-057, Space and Missile Propulsion Div., Edwards AFB, CA, 2003.

[13] Anderson, T. L., *Fracture Mechanics, Fundamentals and Applications*, 2nd ed., CRC Press, Boca Raton, FL, 1995.

[14] Hwang, C., Massa, L., Fiedler, and Geubelle, P., "Simulation of Convective Burning and Dynamic Fracture in Solid Propellants," 38th AIAA/ASME/SAE/ASEE JPC Conference and Exhibit, AIAA Paper 2001-3953, Indianapolis, IN, July 2002.

[15] Kumar, M., and Kuo, K. K., "Effect of Deformation on Flame Spreading and Combustion in Propellant Cracks," *AIAA Journal*, Vol. 19, No. 12, 1981, pp. 1580–1589. doi:10.2514/3.7888

[16] Lu, C., and Kuo, K., "Modeling and Numerical Simulation of Combustion Process Inside a Solid Rocket Propellant Crack," *Propellants, Explosives, Pyrotechnics*, Vol. 19, No. 5, 1994, pp. 217–226. doi:10.1002/prep.19940190502

[17] Lu, Y. C., Kuo, K. K., and Wu, S. R., "Crack Propagation Process in a Burning AP-Based Composite Solid Propellant," AIAA/SAE/ASME/ASEE 29th Joint Propulsion Conference, AIAA 93-2168, June 1993.

[18] Knauss,W. G., "On the Steady Propagation of a Crack in a Viscoelastic Sheet," *Deformation and Fracture of High Polymers*, Plenum, New York, 1974, pp. 501–541.

[19] Shapery, R. A., "Correspondence Principles and a Generalized J Integral for Large Deformation and Fracture Analysis of Viscoelastic Media," *International Journal of Fracture*, Vol. 25, No. 3, 1984, pp. 195–223. doi:10.1007/BF01140837

[20] Shapery, R. A., "A Theory of Crack Initiation and Growth in Viscoelastic Media, Part 2," *International Journal of Fracture*, Vol. 1, No. 3, June 1975, pp. 369–388.

[21] Shapery, R. A., "A Theory of Crack Initiation and Growth in Viscoelastic Media, Part 3," *International Journal of Fracture*, Vol. 11, No. 4, Aug. 1975, pp. 549–562. doi:10.1007/BF00116363

[22] Dugdale, D., "Yielding of Steel Sheets Containing Slits," *Journal of the Mechanics and Physics of Solids*, Vol. 8, 1960, pp. 100–108. doi:10.1016/0022-5096(60)90013-2

[23] Barenblatt, G., "The Mathematical Theory of Equilibrium Crack in the Brittle Fracture," *Advances in Applied Mechanics*, Vol. 7, No. 4, 1962, pp. 55–125.

[24] Buswell, H. J., "An Investigation into Mechanical Failure of Composite Propellants," Ph.D. Dissertation, Univ. of Surrey, Faculty of Mathematical and Physical Sciences, Surrey, England, U.K., 1975.

[25] Swanson, S. R., "Application of Shapery's theory to Viscoelastic Fracture of Solid Propellants," *Journal of Spacecraft and Rockets*, Vol. 13, No. 9, Sept. 1976.

[26] Shapery, R. A., "Time-Dependent Fracture: Continuum Aspects of Crack Growth," *"Encyclopedia of Materials Science and Engineering"*, Pergamon, Oxford, 1986, pp. 5043–5053.

[27] Beckwith, S. W., and Wang, D. T., "Crack Propagation in Double Base Propellants," 16th AIAA Aerospace Sciences Meeting, AIAA Paper 78-170, Jan. 1978.
[28] Bencher, C., Dauskardt, R., and Ritchie, R., "Microstructural Damage and Fracture Processes in a Composite Solid Rocket Propellant," *Journal of Spacecraft and Rockets*, Vol. 32, No. 2, 1995, pp. 328–334. doi:10.2514/3.26614
[29] Langlois, G., and Gonard, R., "New Law for Crack Propagation in Solid Propellant Material," *Journal of Spacecraft and Rockets*, Vol. 16, No. 6, 1979, pp. 357–360. doi:10.2514/3.57674
[30] Liu, C. T., "Microstructural Damage and Crack Growth Behavior in a Composite Solid Propellant," *AGARD PEP Symposium on Service Life of Solid Propellant Systems*, AGARD, Neuilly-sur-Seine, France, 10–14 May 1996.
[31] Smirnov, N. N., and Dimitrienko, I. D., "Convective Combustione Regime in a Deformable Solid Fuel with Longitudinal Channels," *Fizika Goreniya i Vzryva*, Vol. 22, No. 3, May–June 1986, pp. 59–67.
[32] Cervenka, J., Chandra, J., and Saouma, V., "Mixed Mode Fracture of Cementitious Bimaterial Interfaces, Part 2: Numerical Simulation," *Engineering Fracture Mechanics*, Vol. 60, No. 1, 1998, pp. 95–107. doi:10.1016/S0013-7944(97)00094-5
[33] Brühwiler, E., and Saouma, V. E., "Fracture Testing of Rock by the Wedge Splitting Test," *Rock Mechanics Contributions and Challenges*, edited by W. A. Hustrulid, and G. A. Johnson, A. A. Balkema, Rotterdam, The Netherlands, 1990, pp. 287–294.
[34] Slowik, V., Plizzari, G., and Saouma, V., "Fracture of Concrete Under Variable Amplitude Fatigue Loading," *ACI Materials Journal*, Vol. 93, No. 3, 1996, pp. 272–283.
[35] Farris, R. J., "The Influence of Vacuole Formation on the Response and Failure of Highly Filled Elastomers," *Transactions of the Society of Rheology*, Vol. 12, No. 2, 1968, pp. 315–334. doi:10.1122/1.549111
[36] Anon., "STANAG 4507: Explosives, Physical/Mechanical Properties, Stress Relaxation Test in Tension," *NATO Military Agency for Standardization*, Brussels, 2002.
[37] Payne, A. R., "Dynamic Properties of Filler-Loaded Rubbers," *Reinforcement of Elastomers*, Wiley, New York, 1965.
[38] Ferry, J. D., *Viscoelastic Properties of Polymers*, 3rd ed., Wiley, New York, 1980.
[39] Anon., "STANAG 4506: Explosive Materials, Physical/Mechanical Properties, Uniaxial Tensile Test," *NATO Military Agency for Standardization*, Brussels, 2000.
[40] Park, S., "Development of a Nonlinear Thermo viscoelastic Constitutive Equation for Particulate Composites with Growing Damage," Ph.D. Dissertation, Univ. of Texas at Austin, Austin, TX, 1994.
[41] Ozüpek, S., "Constitutive Equations for Solid Propellants," Ph.D. Dissertation, Univ. of Texas at Austin, Austin, TX, 1995.
[42] Schapery, R. A., "A Theory of Mechanical Behavior of Elastic Media with Growing Damage and Other Changes in Structure," *Journal of the Mechanics and Physics of Solids*, Vol. 38, No. 2, 1990.
[43] Anon., "ASTM E399: Standard Test Method for Plane Strain Fracture Toughness of Metallic Materials," Standard E399–74, *Annual Book of ASTM Standards*, ASTM International, Philadelphia, 1974.
[44] Holzapfel, G. A., *Nonlinear Solid Mechanics*, Wiley, New York, 2001.
[45] Saouma, V., Natekar, D., and Hansen, E., "Cohesive Stresses and Size Effects in Elasto-Plastic and Quasi-Brittle Materials," *International Journal of Fracture*, Vol. 119, No. 3, 2003, pp. 287–298. doi:10.1023/A:1023968010028
[46] Kinloch, A. J., and Young, R. J., *Fracture Behaviour of Polymers*, Applied Science Publishers, London, 1983.
[47] Treloar, L. G. R., *The Physics of Rubber Elasticity*, 3rd ed., Clarendon Press, Oxford, 2004.
[48] Hillerborg, A., Modéer, M., and Petersson, P. E., "Analysis of Crack Formation and Crack Growth in Concrete by Means of Fracture Mechanics and Finite Elements," *Cement and Concrete Research*, Vol. 6, No. 6, 1976, pp. 773–782. doi:10.1016/0008-8846(76)90007-7
[49] Bažant, Z. P., "Size Effect in Blunt Fracture: Concrete, Rock, Metal," *Journal of Engineering Mechanics*, Vol. 110, No. 4, 1984, pp. 518–535.
[50] Saouma, V., Natekar, D., and Sbaizero, O., "Nonlinear Finite Element Analysis and Size Effect Study of a Metal-Reinforced Ceramics-Composite," *Materials Science and Engineering A*, Vol. 323, No. 1, 2002, pp. 129–137. doi:10.1016/S0921-5093(01)01360-0

S. Son
Associate Editor